

# Helical magnetorotational instability in a Taylor-Couette flow with strongly reduced Ekman pumping

Frank Stefani<sup>1</sup>, Gunter Gerbeth<sup>1</sup>, Thomas Gundrum<sup>1</sup>, Rainer Hollerbach<sup>2</sup>, Jānis Priede<sup>3</sup>, Günther Rüdiger<sup>4</sup>, and Jacek Szklarski<sup>1,5</sup>

<sup>1</sup>*Forschungszentrum Rossendorf, P.O. Box 510119, D-01314 Dresden, Germany*

<sup>2</sup>*Department of Applied Mathematics, University of Leeds, Leeds, LS2 9JT, United Kingdom*

<sup>3</sup>*Coventry University, Priory Street, Coventry CV1 5FB, United Kingdom*

<sup>4</sup>*Astrophysikalisches Institut Potsdam, An der Sternwarte 16, D-14482 Potsdam, Germany*

<sup>5</sup>*IPPT, ul. Świątokrzyska 21, 00-049 Warsaw, Poland*

The magnetorotational instability (MRI) is thought to play a key role in the formation of stars and black holes by sustaining the turbulence in hydrodynamically stable Keplerian accretion discs. In previous experiments the MRI was observed in a liquid metal Taylor-Couette flow at moderate Reynolds numbers by applying a helical magnetic field. The observation of this helical MRI (HMRI) was interfered with a significant Ekman pumping driven by solid end-caps that confined the instability only to a part of the Taylor-Couette cell. This paper describes the observation of the HMRI in an improved Taylor-Couette setup with the Ekman pumping significantly reduced by using split end-caps. The HMRI, which now spreads over the whole height of the cell, appears much sharper and in better agreement with numerical predictions. By analyzing various parameter dependencies we conclude that the observed HMRI represents a self-sustained global instability rather than a noise-sustained convective one.

PACS numbers: PACS numbers: 47.20.-k, 47.65.+a, 95.30.Qd

## I. INTRODUCTION

Cosmic magnetic fields are produced, on a wide range of spatial scales, by the homogeneous dynamo effect in electrically conducting fluids [1]. The Earth's magnetic field is generated in its outer core, most likely by spiral flow structures which result from the combined action of Coriolis forces and thermal and/or compositional buoyancy [2]. The magnetic field of the Sun is generated in the convection zone and in the tachocline, very likely under the influence of differential rotation and helical turbulence [3]. A similar mechanism is probably at the root of large scale galactic magnetic fields [4], while inter-galactic magnetic fields are thought to be a product of the so-called fluctuation dynamo [5].

Magnetic fields play an active role in cosmic structure formation. It was in 1991 that Balbus and Hawley [6] highlighted the importance of the magnetorotational instability (MRI, or Velikhov-Chandrasekhar instability [7, 8]) for the angular momentum transport in accretion disks around stars and black holes. In MRI, the externally applied magnetic field serves only as a trigger for the instability that actually taps into the rotational energy of the flow. This is quite in contrast to another magnetic instability in which prevailing currents in the fluid can become unstable by themselves. This latter, so-called Tayler instability [9] is held responsible for parts of the dynamo mechanism in stars [10], and for some observed helical structures in jets and outflows [11].

Significant theoretical and computational progress has been made in the understanding of dynamo action and magnetic instabilities. Besides this, the last decade has also seen considerable experimental activities to investigate those effects in the liquid metal laboratory [12, 13]. At the end of 1999, the hydromagnetic dynamo effect was observed nearly simultaneously at the large-scale liquid sodium facilities in Riga [14] and Karlsruhe [15]. In 2006, the VKS-experiment in Cadarache has shown not only self-excitation [16] but also impressive magnetic field reversals [17], although the use of soft-iron impellers with high relative permeability makes the interpretation of these results cumbersome.

As for the so-called “standard MRI” (SMRI), with only an axial magnetic field applied, the authors of [18] claim to have observed it in a spherical Couette flow, but their background state was already fully turbulent, thereby defeating the original idea that the MRI would destabilize an otherwise stable flow.

There is a simple reason for the flow being turbulent before the SMRI sets in. The point is that the azimuthal magnetic field component of the MRI mode can only be produced from the axial field by induction effects, which are proportional to the magnetic Reynolds number ( $Rm$ ) of the flow.  $Rm$ , in turn, is proportional to the hydrodynamic Reynolds number according to  $Rm = PmRe$ , where the magnetic Prandtl number  $Pm = \nu/\lambda$  is the ratio of viscosity  $\nu$  to magnetic diffusivity  $\lambda = 1/\mu_0\sigma$ . For liquid metals  $Pm$  is typically in the range  $10^{-6} \dots 10^{-5}$ . Therefore, in order to achieve  $Rm \sim 1$ , we need  $Re \sim 10^5 \dots 10^6$ , and wall-constrained flows with such high  $Re$  are known to be turbulent, whatever the linear stability analysis might tell. Apparently in contrast with this common wisdom, a group in Princeton has recently shown [19] that a flow profile in a short Taylor-Couette cell can be kept stable until

$Re \sim 10^6$  if an appropriate configuration of split end-caps is used. However, the mechanisms that ultimately leads to flow stabilization in this configuration are not well understood. At least, the optimum rotation ratios of the split rings do not agree with numerical predictions, a discrepancy that might be explained by some wobbling of the inner cylinder [20].

Having learned that  $Rm \sim 1$  (and hence  $Re \sim 10^6$ ) is needed just to produce the azimuthal magnetic field component of the MRI mode from the applied axial field, one might ask why not substitute this induction process by simply *externally applying an azimuthal magnetic field as well?* This idea was pursued in [21, 22], where it was shown that this “helical MRI” (HMRI), as we now call it, is indeed possible at far smaller Reynolds numbers and magnetic field amplitudes than SMRI.

In [21] it was also shown that HMRI and SMRI are continuously connected. In Fig. 1 of [21] the critical  $Rm$  was plotted against the rotation ratio  $\mu := f_{\text{out}}/f_{\text{in}}$  of outer to inner cylinder of a Taylor-Couette set-up. The extremely steep increase of this curve at the Rayleigh line, which occurs for a purely axial magnetic field, is just smeared out when an azimuthal field is added. Although HMRI, in the limit of small  $Re$ , is a weakly destabilized inertial oscillation [23], there is a continuous and monotonic transition to SMRI when  $Re$  and the magnetic field strength are increased simultaneously.

The relation of HMRI, which appears as a travelling wave, and SMRI is currently the subject of intense discussions in the literature [24, 25, 26, 27, 28, 29, 30, 31, 32], the roots of which trace back to an early dispute between Knobloch [33, 34] and Hawley and Balbus [35].

A remarkable property of HMRI for small  $Pm$  (which has been coined “inductionless MRI”), was clearly worked out in [24]. It is the apparent paradox that a magnetic field is able to trigger an instability although the total energy dissipation of the system is larger than without this field. This is not so surprising though when seen in the context of other *dissipation induced instabilities* which are quite common in many areas of physics [36].

Another, and not completely resolved issue concerns the relevance of HMRI for astrophysical flows. On first glance, HMRI seems very attractive as it could extend the range of applicability of MRI into those regions of accretion disks which are characterized by a small  $Pm$ . This might apply to the “dead zones” of protoplanetary disks [37] as well as to the outer parts of accretion disks around black holes [38].

However, before discussing this point in more detail, it has to be checked whether HMRI works at all for Keplerian rotation profiles  $\Omega(r) \sim r^{-3/2}$  or not. In the inductionless limit, i.e. for  $Pm = 0$ , and using a local WKB analysis in the small-gap approximation, the answer to this question is “no” [23]. In contrast to this the solution of the corresponding global eigenvalue equation gives an affirmative answer, as long as at least the outer or the inner radial boundary is electrically conducting [39]. This is certainly good news for the working of HMRI in the outer, cold parts of accretion disks since their inner parts have indeed a higher conductivity.

Unfortunately, even this is not the end of the story. Both methods, the WKB method and the global eigenvalue equation, deal with waves with a single wavenumber and frequency. However, since HMRI appears in the form of a travelling wave, one has to be careful with the interpretation of the positive growth rate of a single monochromatic wave. The crucial point here is that those monochromatic waves are typically not able to fulfill the axial boundary conditions at the ends of the considered region. To fulfill them, one has to consider wave packets. Only wave packets with vanishing group velocity will remain in the finite length system. Typically, the onset of this *absolute instability*, characterized by a zero growth rate *and* a zero group velocity, is harder to achieve than the *convective instability* of a monochromatic wave with zero growth rate. A comprehensive analysis of the relation of convective, absolute, and global instability can be found in the survey papers [40, 41]. In the context of MHD, this distinction played an important role, e.g., in the Riga dynamo experiment [42]. A detailed analysis of the relation of convective and absolute instability for HMRI can be found in [32]. From the extrapolation of the results of this paper it seems that Keplerian rotation profiles are indeed absolutely HMRI-unstable, but a final solution to this puzzle is still elusive.

Notwithstanding these ongoing debates, the dramatic decrease of the critical rotation rates and magnetic field intensities for HMRI, as compared with SMRI, made this new type of MRI particularly attractive for experimental studies.

First experimental evidence for HMRI was obtained in 2006 at the liquid metal facility PROMISE (*Potsdam ROssendorf Magnetic InStability Experiment*) which is basically a Taylor-Couette (TC) cell made of concentric rotating copper walls, filled with GaInSn (a eutectic which is liquid at room temperatures). In [43] it was shown that the MRI travelling wave appears only in the predicted finite window of the magnetic field intensity, with a frequency of the travelling wave that was also in good accordance with numerical simulations. More detailed results were published in [44, 45].

However, a slight difficulty with these early experiments was the fact that the MRI wave did not travel along the entire height of the Taylor-Couette cell but ceased to exist at some position typically close to mid-height. By modifying slightly the electric boundary conditions in radial direction, and analyzing the resulting change of the axial velocity [46], it was possible to identify this sink of the travelling wave with the position of the radial jet that originates from the Ekman pumping at the upper and lower lids of the TC cell [47]. The influence of this Ekman pumping on the

flow structure was extensively discussed in a number of papers [25, 27, 28].

A related critical point is connected with electric currents which are induced in the lower end-cap that was made of copper in the first PROMISE experiments (now called PROMISE 1). In the worst case these currents are able to drive a significant Dean flow which possibly could modify the original Taylor-Couette flow profile [27, 48].

In order to overcome both problems we have changed the axial boundary conditions, first by replacing the copper of the lower lid by insulating material, and second by splitting the (upper and lower) lids into two rings (rotating with the inner and outer cylinder, respectively) in order to minimize the Ekman pumping. Henceforth, this new version of the experiment will be called PROMISE 2 in order to discriminate it from the previous PROMISE 1 experiment.

In this paper we will show that the minimization of the Ekman pumping makes the radial jet disappear almost completely. Consequently, the MRI wave can travel throughout the entire TC cell. We will investigate in detail four parameter dependencies of the MRI wave showing a much improved agreement with the 2D numerical predictions. Further comparisons with the results of a 1D eigenvalue code for the convective and absolute instability will provide strong evidence that the observed wave represents a global instability and not only a noise-triggered convective instability as argued in [26, 31].

## II. FROM PROMISE 1 TO PROMISE 2

Apart from the modified end-caps, the PROMISE 2 set-up is more or less identical to that of PROMISE 1 which was described in detail in [43, 45]. Its main part is a cylindrical vessel (cp. Fig. 1) made of two concentric copper cylinders. The inner one is 10 mm thick extending in radius from 22 to 32 mm; the outer wall is 15 mm thick, extending from 80 to 95 mm in  $r$ . This vessel is filled with the eutectic alloy  $\text{Ga}^{67}\text{In}^{20.5}\text{Sn}^{12.5}$  whose physical properties at 25°C are as follows: density  $\rho = 6.36 \times 10^3 \text{ kg/m}^3$ , kinematic viscosity  $\nu = 3.40 \times 10^{-7} \text{ m}^2/\text{s}$ , electrical conductivity  $\sigma = 3.27 \times 10^6 (\Omega \text{ m})^{-1}$ . The magnetic Prandtl number is then  $Pm = \mu_0 \sigma \nu = 1.40 \times 10^{-6}$ .

The copper vessel is closed by a plastic bottom and is fixed, via an aluminum spacer, on a precision turntable; the outer wall of the vessel thus serves as the outer cylinder of the TC cell. The inner cylinder of the TC flow is fixed to an upper turntable, and is immersed into the liquid metal from above. It has a thickness of 4 mm, extending in radius from 36 to 40 mm. Between this immersed cylinder and the inner wall of the containment vessel there is thus a gap of 4 mm, also filled with GaInSn. The actual TC cell then extends in radial direction over a cylindrical gap of width  $d = r_{\text{out}} - r_{\text{in}} = 40 \text{ mm}$  from the outer surface of the inner cylinder at  $r_{\text{in}} = 40 \text{ mm}$  to the inner surface of the outer wall of the containment vessel at  $r_{\text{out}} = 80 \text{ mm}$ , and in axial direction over the liquid metal height of  $0 \text{ mm} \leq z \leq 400 \text{ mm}$ .

While in PROMISE 1 the upper end-cap was a plastic lid fixed to the outer frame this end-cap is now split into two concentric plastic rings (see Fig. 2). The inner ring rotates with the inner copper cylinder, the outer one rotates with the outer cylinder. By this means, the opposing Ekman pumping effects at the rings compensate each other to a large extent. The choice of the splitting position at  $r = 56 \text{ mm}$  was motivated by the simulation in [27] showing that a splitting at  $0.4 d$  would minimize the global Ekman pumping for the case with the two rings attached to the cylinders (using only two rings significantly simplifies the construction when compared to a many-rings case). The lower end-cap is split in the same manner, so that we have a symmetric configuration, with respect to both the rotation rate and to the electrical conductivities. This is a significant improvement compared with PROMISE 1, in which the copper bottom was simply part of the vessel which rotated with the outer cylinder.

The magnetic field configuration is identical to that of PROMISE 1, with axial magnetic fields of order 10 mT being produced by the current  $I_{\text{coil}}$  in a double-layer coil with 78 windings, and an azimuthal field of the same order being generated by a current  $I_{\text{rod}}$  through a central water-cooled copper rod of radius 15 mm.

As in PROMISE 1, the measuring instrumentation consists exclusively of two high-focus ultrasonic transducers (from Signal Processing SA) with a working frequency of 4 MHz which are fixed into the outer plastic ring, 12 mm away from the outer copper wall, flush mounted at the interface to the GaInSn. Since this outer ring is rotating, it is necessary to transfer the signal into the laboratory frame (in contrast to PROMISE 1 in which the upper lid was fixed to the frame). This is accomplished by the use of a slip ring contact which is situated below the TC vessel (not shown in Fig. 1).

The advantage of the Ultrasound Doppler Velocimetry (UDV) is that it provides full profiles of the axial velocity  $v_z$  along the beam-lines parallel to the axis of rotation. The spatial resolution in axial direction is chosen 0.685 mm, the time resolution is 1.84 sec. The width of the beam (over which  $v_z$  is averaged) is approximately 8 mm, according to the diameter of the ultrasonic transducers.

To get reliable signals from along the 400 mm height of the TC cell one has to ensure a good acoustic contact between the transducer and the GaInSn which is often compromised by non-perfect wetting, sticking oxides or bubbles. A good signal is all the more important since the velocity perturbations to be measured are typically in the order of 0.1 mm/s, which is at the lower edge of the applicability of the UDV technique.

This fact has to be kept in mind when comparing, i.e., rms values of the velocity perturbation from different runs. For example, the identification of the transition between stable and unstable regimes rely strongly on the measured velocity distribution. However, this velocity signal is typically affected by noise which, in turn, depends on the acoustic contact.

Typically, the duration of the experimental runs was 1900 sec, after a waiting time of one hour or even longer in cases when long transients were to be expected.

### III. RESULTS

In this section, we will present the main experimental results and compare them with numerical results based on a 1D eigenvalue solver (for details consult [24, 32]) and on a time-stepping 2D solver that was already used in [27]. Usually, for both solvers perfectly conducting boundary conditions were applied at the inner and outer radius, which is certainly not completely correct since the conductivity of copper is approximately 13 times higher than that of GaInSn, but not infinite. For some parameters, at least, it has been checked that the inclusion of the finite-thickness copper walls in the 1D eigenvalue code does not change significantly the results based on perfectly conducting walls.

In particular we will study the dependence of the HMRI on the four parameters that govern the problem. Given the inner and outer radii of the TC cell,  $r_{\text{in}}$  and  $r_{\text{out}}$  (with a gap width  $d = r_{\text{out}} - r_{\text{in}}$ ), the rotation rate of inner and outer cylinder,  $f_{\text{in}}$  and  $f_{\text{out}}$ , the axial magnetic field  $B_z$  and and the azimuthal magnetic field at the inner cylinder,  $B_\varphi(r = r_{\text{in}})$ , these governing parameters are the Reynolds number

$$Re := 2\pi f_{\text{in}} d / \nu, \quad (1)$$

the ratio of rotation rates

$$\mu := f_{\text{out}} / f_{\text{in}}, \quad (2)$$

the Hartmann number

$$Ha := B_z (r_{\text{in}} d \sigma / \rho \nu)^{1/2}, \quad (3)$$

and the ratio of azimuthal to axial magnetic field

$$\beta := B_\varphi(r = r_{\text{in}}) / B_z. \quad (4)$$

With the actual geometry and the material properties of GaInSn given, we can derive the following useful relations between the experimental parameters and the dimensionless parameters:

$$Re = 29586 \cdot f_{\text{in}} / \text{Hz}, \quad (5)$$

$$Ha = 0.158 \cdot I_{\text{coil}} / \text{A}, \quad (6)$$

$$\beta = 0.0491 \cdot I_{\text{rod}} / I_{\text{coil}}. \quad (7)$$

Before entering into the details of the parameter dependencies of the MRI, we present the results in the magnetic field free case.

#### A. Results without magnetic fields

The flow structure in the non-magnetic case is an important reference point for the later analysis of the MRI. Starting with  $\mu = 0$ , we expect a Taylor vortex flow (TVF) whose amplitude decreases for increasing  $\mu$ . Beyond the Rayleigh point  $\mu_{\text{Rayl}} := r_{\text{in}}^2 / r_{\text{out}}^2 = 0.25$ , the TVF is supposed to disappear completely in accordance with Rayleigh's criterion. However, in any real TC-cell with finite height this is far from trivial due to the existence of a meridional flow driven by the Ekman pumping at the upper and lower lids. Approximately at mid-height of the TC cell the two opposed vertical flows meet each other and produce a radial jet [47].

The difference of the flows in the PROMISE 1 and PROMISE 2 configuration, respectively, is documented in Fig. 3. What is actually shown is the velocity component measured along the ultrasonic beam-lines. This velocity component is supposed to represent the total axial velocity  $V_z(z, t)$ , although some slight influence of the strongly dominant  $V_\varphi$

component cannot be ruled out in case the direction of the UDV transducers is not perfectly vertical. On the r.h.s. of each panel the time-averaged value  $va_z(z)$  is given in dependence on the axial position  $z$ .

Figure 3 shows, at  $f_{\text{in}} = 0.1$  Hz, the results for PROMISE 2, (a), (b), and (c) corresponding to  $\mu = 0$ ,  $\mu = 0.1$ , and  $\mu = 0.27$ , respectively. As expected, we observe a TVF which is getting weaker for increasing  $\mu$  and which disappears completely at  $\mu = 0.27$ . For comparison, Fig. 3d shows one result for PROMISE 1, at  $f_{\text{in}} = 0.06$  Hz and  $\mu = 0.27$ . Here we observe a very steep sign change of  $V_z(z)$  approximately at mid-height which necessarily must be connected with a radial jet at this point, a feature that is nearly absent in PROMISE 2 (Fig. 3c). Evidently the global effect of the Ekman pumping is drastically reduced by the splitting of the end-caps. In the following we will see that this absence of the radial jet has important consequences for the propagation of the MRI wave.

## B. Variation of $Re$

As with many other instabilities in hydrodynamics, MRI is expected to set in at a certain critical Reynolds number  $Re_{\text{crit}}$ . In order to study this transition in detail, we have fixed the rotation ratio to  $\mu = 0.27$  and the current through the coil to  $I_{\text{coil}} = 76$  A (i.e.  $Ha = 12$ ). The current through the central rod has been set to either  $I_{\text{rod}} = 4000$  A (i.e.  $\beta = 2.59$ ) or  $I_{\text{rod}} = 7000$  A (i.e.  $\beta = 4.53$ ). Throughout the paper (if not otherwise stated) we have chosen the rotation to be clockwise, when viewed from above, and  $B_z$  and  $I_{\text{rod}}$  directed downward, where the latter induces  $B_\varphi$  in the clockwise direction.

To start with, we show in Fig. 4 the axial velocity signals, again the time averaged  $va_z(z)$  on the r.h.s, but here and henceforth the deviation  $v_z(z, t) := V_z(z, t) - va_z(z)$  of the total velocity from the time averaged value on the l.h.s. The panels (a) and (b) exhibit the individual signals from the UDV sensors 1 and 2, respectively, (c) shows their average, and (d) shows their difference. Actually, in this difference signal one observes a slight  $m = 1$  mode with a dominant frequency equal to the rotation rate of the outer cylinder, which results just from some slight asymmetries of the facility (e.g. the current leads to the central rods). This is in contrast to PROMISE 1 where we have observed, in some parameter regions [43, 45, 46], an  $m = 1$  mode with a frequency between the rotation rate of inner and outer cylinder whose origin is not yet clarified.

For  $I_{\text{rod}} = 7000$  A and  $I_{\text{coil}} = 76$  A, the 12 panels of Fig. 5 show  $V_z(z, t)$  for increasing  $f_{\text{in}}$  (i.e.  $Re$ ). From here on, the l.h.s. of each panel exhibits the average over the two sensors (corresponding to panel (c) in Fig. 4). Evidently, the travelling wave instability sets in approximately between  $f_{\text{in}} = 0.04 \dots 0.05$  Hz (i.e.  $Re = 1183 \dots 1479$ ) and remains until the highest value  $f_{\text{in}} = 0.24$  Hz (i.e.  $Re = 6830$ ) that we have studied in the experiment.

It is also instructive to see what happens when we change the direction of  $B_z$  by changing the direction of the current in the coil. It is well-known that the direction of propagation, i.e. whether the wave pattern drifts in the  $+z$  or  $-z$  direction, depends on whether the product  $\Omega B_z B_\varphi$  is negative or positive, respectively. Figure 6 documents this effect for the parameter choice  $f_{\text{in}} = 0.1$  Hz,  $\mu = 0.27$ ,  $I_{\text{rod}} = 7000$  A, and  $I_{\text{coil}} = \pm 76$  A. Note that the shape of the (a) upward and (b) downward travelling wave is now quite symmetric, in contrast to PROMISE 1 in which the position of the radial jet made the pattern more asymmetric (see, e.g. Fig. 4 in [46]).

When speaking about upward and downward travelling wave it is also necessary to say that these two types do not appear exclusively. Actually, the upward travelling wave, when reflected at the upper boundary, produces a slight downward travelling wave, and vice versa. To analyze this point we show in Fig. 7 the 2D Fourier transform from the  $z, t$ -space to the  $k, f$ -space of the signal  $v_z(z, t)$  for  $f_{\text{in}} = 0.05$  Hz. Not surprisingly, the experimental data are more smeared out than the numerical predictions. Nevertheless, the position of the maximum in the  $k, f$  space is approximately the same in both cases. The maximum of the 2D FFT is mainly localized in the second and fourth quadrant of the  $k, f$ -space which indicates an upward travelling wave. However, the slight signal in the first and third quadrant indicates also the existence of a downward travelling wave.

By applying a Hilbert transform to the original data, it is possible to disentangle the dominant upward travelling wave and the minor downward travelling wave which results from a reflection of the upward travelling wave at the upper end-cap. This is done, now again for  $f_{\text{in}} = 0.1$  Hz,  $\mu = 0.27$ , in Fig. 8. Inspired by [50], we will later use the ratio of the maxima of the downward to the upward travelling wave as an additional indicator for the onset of the absolute instability.

In Fig. 9 we restrict ourselves to the downward travelling wave and compare its shape with simulated results for the particular cases  $f_{\text{in}} = 0.04$  Hz and  $f_{\text{in}} = 0.05$  Hz. We observe a quite convincing agreement of experimental data and numerical simulation, even the amazing slow decay of a transient wave at  $f_{\text{in}} = 0.04$  Hz is recovered by the numerics.

A more quantitative comparison of various experimentally and numerically obtained features of the MRI wave, in dependence on  $f_{\text{in}}$ , is made in Fig. 10. This figure contains four parts: Fig. 10a shows the squared rms of  $v_z(z, t)$ , calculated between  $250 \text{ mm} < z < 350 \text{ mm}$  (this particular range has been chosen since the velocity in this interval is comparably high and the UDV signal is usually not much affected by noise as it is for smaller values of  $z$ ). Figure 10b shows the squared ratio of the maximum amplitude (taken over all  $z$ ) of the downward to that of the upward

travelling wave. This quantity had been used successfully in other problems to distinguish between absolute and convective instability [50]. Figures 10c and 10d show the normalized wave frequency  $f_{\text{wave}}/f_{\text{in}}$  and the normalized phase velocity of the wave  $c_{\text{wave}}/(f_{\text{in}}r_{\text{in}})$ , respectively. The same dependencies, but now in more detail for  $0.02 \text{ Hz} < f_{\text{in}} < 0.1 \text{ Hz}$  are shown in Fig. 11.

Basically, the agreement between experiment and numerical results from the 2D code is quite convincing, in particular the onset of the instability approximately at  $f_{\text{in}} = 0.4 \text{ Hz}$  for  $I_{\text{rod}} = 7000 \text{ A}$ . However, there is one significant deviation: while the numerics indicate a disappearance of the instability approximately at  $f_{\text{in}} = 0.11 \text{ Hz}$ , the experiment shows a continuation of the instability far beyond this point. The reason of this difference is not yet clear. What can be said, at least, is that the chosen parameter  $\mu = 0.27$  is very close to the maximum value of  $\mu$  beyond which HMRI ceases to exist. Here, the instability is extremely sensitive, and any slight deviation of the experimental conditions from the numerical assumptions can play a significant role.

For  $I_{\text{rod}} = 4000 \text{ A}$ , the amplitude of the velocity is very small in good accordance with the numerics which predicts stability for all values of  $Re$ .

As noted in the introduction, the importance of MRI lies in the fact that it destabilizes rotational flows with outward increasing angular momentum which would otherwise be hydrodynamically stable, according to Rayleigh's criterion. Doing experiments on MRI it is necessary to validate that the angular momentum of the base flow is indeed increasing outward. This is all the more important since a peculiarity of HMRI at small Reynolds and Hartmann numbers is that it works only for values of  $\mu$  which are slightly above the Rayleigh line. Since, in a finite system, some deviation from the ideal TC-flow profile is unavoidable, in particular close to the end-caps, one has to be careful that the observed instability is indeed a magnetically triggered one and not an instability of a flow which is (at least in some parts) hydrodynamically unstable.

Unfortunately, the UDV technique allows us only to measure axial velocity distributions in detail. Some efforts have been made to measure  $V_\varphi$  by means of an electric potential probe inserted into the liquid metal, but neither the necessary accuracy nor the desired spatial resolution could be achieved by this method. For that reason we have to rely on the numerical simulations exclusively. Given the good correspondence of numerics and experiment, as seen so far in the  $V_z$  data (at least for not too high values of  $Re$ ), we believe that the numerics gives a more or less true picture of the real physical process.

In the following we will consider the particular case  $\mu = 0.27$ ,  $I_{\text{coil}} = 76 \text{ A}$ ,  $I_{\text{rod}} = 7000 \text{ A}$  with two different values of  $f_{\text{in}} = 0.04 \text{ Hz}$  (corresponding to  $Re = 1183$ ), and  $f_{\text{in}} = 0.05 \text{ Hz}$  (corresponding to  $Re = 1479$ ). For these two cases we plot in Fig. 12 the numerical snapshots of the angular velocity  $\Omega(r, z)$ , of the specific angular momentum  $r^2\Omega(r, z)$ , and of the radial derivative of this specific angular momentum.

While the plots for  $\Omega(r, z)$  (Fig. 12a) are not very instructive and seem to indicate only a slight difference between the two cases, the plots for the angular momentum and its radial derivative show considerably more structure. For  $f_{\text{in}} = 0.04 \text{ Hz}$  we observe a rather regular outward increase of the angular momentum, with the only exception close to the splitting positions of the upper and lower end-caps. This is not surprising since, with the inner ring rotating with the (fast) inner cylinder and the outer ring rotating with the (slow) outer cylinder, there must be a certain region where the angular momentum decreases, while in the rest of the fluid it increases outward.

The crucial point here is the transition from global stability to global instability when going from  $f_{\text{in}} = 0.04 \text{ Hz}$  to  $f_{\text{in}} = 0.05 \text{ Hz}$ . For the latter we observe a wave that travels throughout the total volume of the TC cell. Clearly visible is the ‘‘fingering’’ of the angular momentum which is typical for MRI [51].

### C. Variation of $\mu$

Without any magnetic field, the case  $\mu = 0$  corresponds to the classical TC flow with its well-known critical Reynolds number  $Re_{\text{crit}} = 68.2$  (for our particular case  $r_{\text{in}}/r_{\text{out}} = 0.5$ ) [52]. With a purely axial or a purely azimuthal field applied this critical value would increase. If both field are applied, the character of the instability changes from a steady TVF to a travelling wave, although with a very small frequency. If  $\mu$  is then increased, the wave frequency increases also. HMRI means that the travelling wave continues into the region beyond the Rayleigh point  $\mu_{\text{Rayl}} := r_{\text{in}}^2/r_{\text{out}}^2 = 0.25$  where any purely hydrodynamic instability would disappear according to Rayleigh's criterion.

For the PROMISE 1 experiment the behaviour of the wave with increasing  $\mu$  was documented in Fig. 5 of [45]. It was characterized by a rather broad range of instability extending to values as large as  $\mu = 0.35$ . Here we present the corresponding results for the PROMISE 2 experiment. Figure 13 shows 12 panels for  $0 < \mu < 0.35$ . We have fixed  $f_{\text{in}} = 0.1 \text{ Hz}$ ,  $I_{\text{coil}} = 76$  (i.e.  $Ha = 12$ ). The current through the central rod has been set to  $I_{\text{rod}} = 7000 \text{ A}$  (i.e.  $\beta = 4.53$ ). It is clearly visible that the travelling wave continues beyond the Rayleigh line, though not very far. At  $\mu = 0.32$  it has disappeared completely.

The comparison of the upward travelling wave for  $\mu = 0.26$  and  $\mu = 0.27$  is illustrated in Fig. 14. Figures 15 and 16 show again the squared rms of the velocity, the squared ratio of the upward and downward travelling wave, the

wave frequency and the wave speed. In addition to the results of a time-stepping 2D solver we have also added the critical  $\mu$  values for the convective and the absolute instability as they result from a 1D eigenvalue solver [32].

Besides the good agreement of experimental and numerical results from the 2D code, it is most remarkable that the transition point from the 2D code corresponds quite accurately to the absolute instability from the 1D simulation, while the 1D results for the convective instability lie at much too high  $\mu$  values. This is strong evidence that the observed instability is a global one and not only a noise-triggered convective one as claimed in [31].

#### D. Variation of $\beta$

For liquid metals with  $Pm = 10^{-6} \dots 10^{-5}$ , the critical Reynolds number for SMRI (with a purely axial magnetic field) is in the order of several million. The key point of HMRI is that by adding an azimuthal magnetic field, this number drops drastically to approximately  $10^3$ . For PROMISE 1, the transition to instability for increasing  $\beta$  turned out to be not very sharp, as documented in [44]. In the following we will investigate the corresponding transition for PROMISE 2.

Figure 17 shows 12 panels for  $0 < I_{\text{rod}} < 8200$  A. Evidently, there is no indication of any instability for  $I_{\text{rod}} < 3000$  A. The transition to MRI occurs approximately between  $I_{\text{rod}} = 4000$  and  $I_{\text{rod}} = 5000$ . The comparison with the numerical simulation for  $I_{\text{rod}} = 4500$  A and  $I_{\text{rod}} = 7000$  A is shown in Fig. 18.

Figure 19 shows again the quantitative analysis for two different lines corresponding to  $\mu = 0.26$  and  $\mu = 0.27$ . The first noticeable fact is that for  $\mu = 0.26$  we obtain, quite similar to the case of the  $\mu$  line discussed above, a good agreement of the 1D numerical results for the absolute instability and the 2D simulation, while the 1D code results for the convective instability would point to much smaller values of the critical  $\beta$ . Quite interesting, however, is the fact that for  $\mu = 0.27$  the agreement of absolute instability (at  $I_{\text{rod}} \sim 8200$  A) and global instability ( $I_{\text{rod}} \sim 7000$  A) becomes worse. Evidently, the value  $\mu = 0.27$  is (at least for the given  $Ha$  number) very close to the upper limit of the HMRI. In this case, the threshold of MRI will be extremely sensitive to any slight modification of the base  $V_\varphi(r)$  profile. This is a typical case in which we indeed observe a global instability for the experimental axial boundary conditions, but the hypothetical use of ideal Taylor-Couette boundary conditions would make the flow stable again. This interesting case has been observed in the numerical simulations of Liu ([26] for PROMISE 1, [31] for PROMISE 2). However, as we see here the interpretation of the author is not correct: what is observed for real boundary conditions is not a noise-induced convective instability (this would start already at  $\beta = 2.3$ ) but still a global instability, although on the basis of a flow that is slightly modified by the lids which make the flow a bit more prone to MRI than the ideal TC-flow would be.

#### E. Variation of $Ha$

MRI is a weak field instability characterized not only by a lower critical  $Ha$  but also by an upper one. For the PROMISE 1 experiment it had been shown in [43] that the travelling wave appears approximately at a coil current 30 A and disappears again at 110 A.

Here we discuss the corresponding behaviour for PROMISE 2. We choose  $f_{\text{in}} = 0.06$  Hz,  $\mu = 0.27$ , and study in detail the cases  $I_{\text{rod}} = 7000$  A and  $I_{\text{rod}} = 8000$  A. Figures 20, 21, and 22 document again the MRI dependence on  $I_{\text{coil}}$  (i.e.  $Ha$ ), the comparison with numerics, and the quantitative analysis, respectively. While the transition between stable and unstable regime for large  $Ha$  numbers (around 15) shows a satisfactory agreement of experiment and numerics, this agreement becomes worse for the transition at low  $Ha$  numbers. Actually, the observed MRI starts already at lower  $Ha$  (around 4...5) in contrast to the theory which predicts it to start between 8 and 9. This effect needs further work to be understood.

Similar as for the  $\beta$ -line (at  $\mu = 0.27$ ) in the former subsection, we have to note that the absolute instability would only start slightly beyond the chosen rod-current of 8000 A. We obtain, nevertheless a global instability which points to a slight modification of the base flow.

### IV. CONCLUSIONS

In this paper we have documented and analyzed four types of parameter variations in order to characterize in detail the HMRI in a TC-flow with split end-caps (PROMISE 2). Due to the strongly reduced Ekman pumping, resulting from this apparently minor modification, we have observed much sharper transitions from the stable flow regime to the MRI regime than in the former PROMISE 1 experiment.

In general, the experimentally observed thresholds turned out to be in good correspondence with the thresholds resulting from 2D simulations for the global instability. In addition to that, we have shown that the results of a 1D eigenvalue solver for the absolute instability are in good agreement with the global instability, at least as long as we are not too close to some upper limit values of  $\mu$  (approximately 0.27 for the considered values of  $Re$ ,  $Ha$  and  $\beta$ ) for the occurrence of HMRI.

In contrast to that, the convective instability resulting from the 1D code would generally imply a larger range of the instability than observed in the experiment. From this it seems justified to conclude that the observed instability is indeed a global one which corresponds, in a wide range of parameters, to the absolute instability and not to a noise-driven convective one.

Coming closer to those parameters (in particular  $\mu$ ) for which helical MRI ceases to exist (at least for the achievable values of  $Ha$  and  $\beta$ ) we observe increasing deviations between global and absolute instability, which very likely trace back to the slightly changed velocity profile of the base flow in the finite TC-cell.

What is left for future work is a careful comparison of the  $z$ -dependence of the wave amplitude with the corresponding results of the 2D code and of the 1D eigenvalue code (in which this  $z$ -dependence appears as an imaginary part of the wavenumber). Comparisons for a few parameters seem to indicate a fairly good agreement, but a quantitative comparison for all parameter variations requires much more work.

A “promising” perspective of PROMISE would be to extend the range of parameters  $Re$  and  $Ha$  in order to investigate the continuous transition between the well-studied region of HMRI and the experimentally much more demanding region of SMRI. One way to accomplish this would be to replace the working fluid GaInSn by sodium. Another interesting extension of the work would be to study various combinations of MRI and Tayler instability, which would require to direct electric currents through the liquid metal. The most interesting idea, however, namely to realize in experiment a self-sustaining nonlinear dynamo process in an MRI-destabilized (quasi)-Keplerian shear flow [53], will probably remain a dream, at least for liquid metal flows. Some appropriate plasma experiments [54] may be better suited for such an ambitious project.

### Acknowledgments

This work was supported by the German Leibniz Gemeinschaft, within its Senatsausschuss Wettbewerb (SAW) programme, and by the Deutsche Forschungsgemeinschaft in the framework of SFB 609.

- 
- [1] G. Rüdiger and R. Hollerbach, *The Magnetic Universe* (Wiley, Berlin 2004).
  - [2] D.J. Stevenson, *Earth Planet. Sci. Lett.* **208**, 1 (2003).
  - [3] M. Ossendrijver, *Astron. Astrophys. Rev.* **11**, 287 (2003).
  - [4] A. Brandenburg and K. Subramanian, *Phys. Rep.* **417**, 1 (2005).
  - [5] A.A. Schekochihin and S.C. Cowley, *Phys. Plasmas* **13**, 056501 (2006)
  - [6] S.A. Balbus and J. F. Hawley, *Astrophys. J.* **376**, 214 (1991).
  - [7] E.P. Velikhov, *Sov. Phys. JETP* **36**, 995 (1959).
  - [8] S. Chandrasekhar, *Proc. Natl. Acad. Sci.* **46**, 253 (1960).
  - [9] R.J. Tayler, *Mon. Not. R. Astron. Soc.* **161**, 365 (1973).
  - [10] H.C. Spruit, *Astron. Astrophys.* **381**, 923 (2002).
  - [11] R. Moll, H.C. Spruit, and M. Obergaulinger, *Astron. Astrophys.* **492**, 621 (2008).
  - [12] A. Gailitis, O. Lielausis, E. Platacis, G. Gerbeth, and F. Stefani, *Rev. Mod. Phys.* **74**, 973 (2002).
  - [13] F. Stefani, A. Gailitis, and G. Gerbeth, *ZAMM* **88**, 930 (2008).
  - [14] A. Gailitis et al., *Phys. Rev. Lett.* **84**, 4365 (2000)
  - [15] R. Stieglitz and U. Müller, *Phys. Fluids* **13**, 561 (2001).
  - [16] R. Monchaux et al., *Phys. Rev. Lett.* **98**, 044502 (2007).
  - [17] M. Berhanu et al., *EPL* **77**, 59001 (2007).
  - [18] D.R. Sisan, N. Mujica, W.A. Tiltonson, Y.M. Huang, W. Dorland, A.B. Hassam, T.M. Antonsen, and D.P. Lathrop, *Phys. Rev. Lett.* **93**, 114502 (2004).
  - [19] H.T. Ji, M. Burin, E. Schartman, and J. Goodman, *Nature* **444** 343 (2006).
  - [20] A. Roach, H. Ji, W. Liu, and J. Goodman, *Bull. Amer. Phys. Soc.* **52**, No. 11, BP8.00084 (2007).
  - [21] R. Hollerbach and G. Rüdiger, *Phys. Rev. Lett.* **95**, 124501 (2005).
  - [22] G. Rüdiger, R. Hollerbach, M. Schultz, and D.A. Shalybkov, *Astron. Nachr.* **326**, 409 (2005).
  - [23] W. Liu, J. Goodman, I. Herron, and H. Ji, *Phys. Rev. E* **74**, 056302 (2006).
  - [24] J. Priede, I. Grants, and G. Gerbeth, *Phys. Rev. E* **75**, 047303 (2007).
  - [25] J. Szklarski and G. Rüdiger, *Astron. Nachr.* **327**, 844 (2006).

- [26] W. Liu, J. Goodman, and H. Ji, Phys. Rev E **76**, 016310 (2007).
- [27] J. Szklarski, Astron. Nachr. **328**, 499 (2007).
- [28] J. Szklarski and G. Rüdiger, Phys. Rev. E **76**, 066308 (2007).
- [29] V.P. Lakhin and E.P. Velikhov, Phys. Lett. A **369**, 98 (2007).
- [30] J. Szklarski and G. Gerbeth, Astron. Nachr. **329**, 667 (2008).
- [31] W. Liu, Astrophys. J. **692**, 998 (2009).
- [32] J. Priede and G. Gerbeth, Phys. Rev E (in press); e-print arXiv:0810.0386
- [33] E. Knobloch, Mon. Not. R. Astron. Soc. **255**, P25 (1992).
- [34] E. Knobloch, Phys. Fluids **8**, 1446 (1996).
- [35] J.F. Hawley and S.A. Balbus, Astrophys. J. **400**, 595 (1992).
- [36] R. Krechetnikov and J.E. Marsden, Rev. Mod. Phys. **79**, 519 (2007).
- [37] N.J. Turner, T. Sano, and N. Dziourkevitch, Astrophys. J. **659**, 729 (2007).
- [38] S.A. Balbus and P. Henri, Astrophys. J. **674**, 408 (2008).
- [39] G. Rüdiger and R. Hollerbach, Phys. Rev. E. **76**, 068301 (2007).
- [40] P. Huerre and P.A. Monkewitz, Ann. Rev. Fluid Mech. **22**, 473 (1990).
- [41] J.M. Chomaz, Ann. Rev. Fluid Mech. **37**, 357 (2005).
- [42] A. Gailitis and Y. Freibergs, Magnetohydrodynamics **16**, 116 (1980).
- [43] F. Stefani, Th. Gundrum, G. Gerbeth, G. Rüdiger, M. Schultz, J. Szklarski, and R. Hollerbach, Phys. Rev. Lett. **97**, 184502 (2006).
- [44] G. Rüdiger, R. Hollerbach, F. Stefani, Th. Gundrum, G. Gerbeth, and R. Rosner, Astrophys. J. **649**, L145 (2006).
- [45] F. Stefani, Th. Gundrum, G. Gerbeth, G. Rüdiger, J. Szklarski, and R. Hollerbach, New J. Phys. **9**, 295 (2007).
- [46] F. Stefani, G. Gerbeth, Th. Gundrum, J. Szklarski, G. Rüdiger, and R. Hollerbach, Astron. Nachr. **329**, 652 (2008).
- [47] A. Kageyama, H. Ji, J. Goodman, F. Chen, and E. Shoshan, J. Phys. Soc. Jpn. **73**, 2424 (2004).
- [48] J. Priede, e-print arXiv:0902.4896
- [49] F. Stefani, G. Gerbeth, Th. Gundrum, J. Szklarski, G. Rüdiger, and R. Hollerbach, e-print arXiv:0812.3790.
- [50] N. Garnier and A. Chiffaudel, Phys. Rev. Lett. **86**, 75 (2001).
- [51] B. Jamroz, K. Julien, and E. Knobloch, Physica Scripta **T132**, 014027 (2008).
- [52] S. Chandrasekhar, *Hydrodynamic and hydromagnetic instability* (Dover, New York 1981).
- [53] F. Rincon, G.I. Ogilvie, and M.R.E. Proctor, Phys. Rev. Lett. **98**, 254502 (2007).
- [54] E.J. Spence, K. Reuter, and C.B. Forest, e-print arXiv:0901.3406.

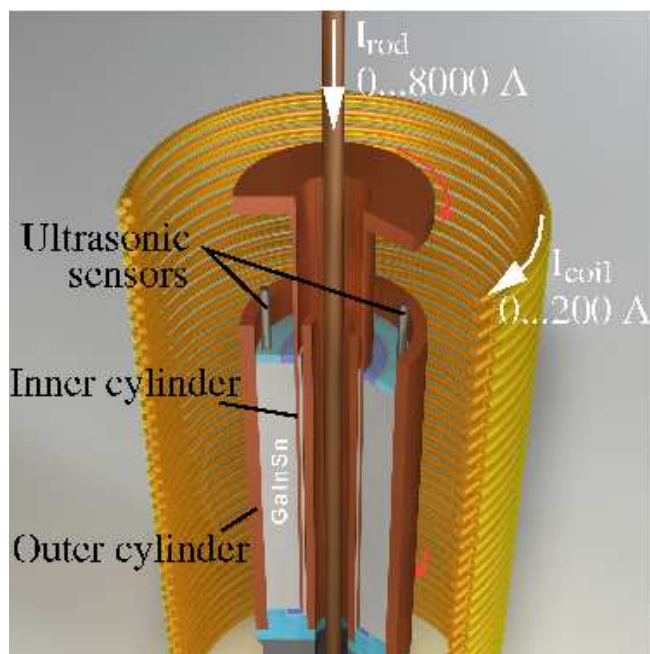


FIG. 1: Sketch of the PROMISE 2 experiment. The gap width of the Taylor-Couette cell is 40 mm, the height is 400 mm.

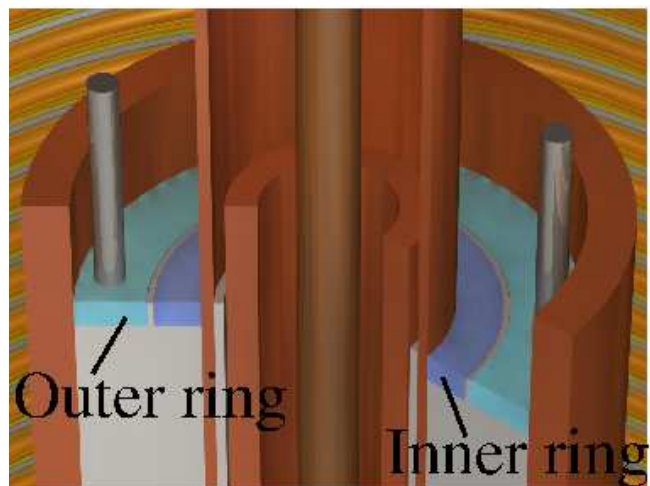


FIG. 2: Details of the PROMISE 2 experiment at the top. The inner ring rotates with the inner cylinder, the outer ring rotates with the outer cylinder. The same applies to the end-cap at the bottom.

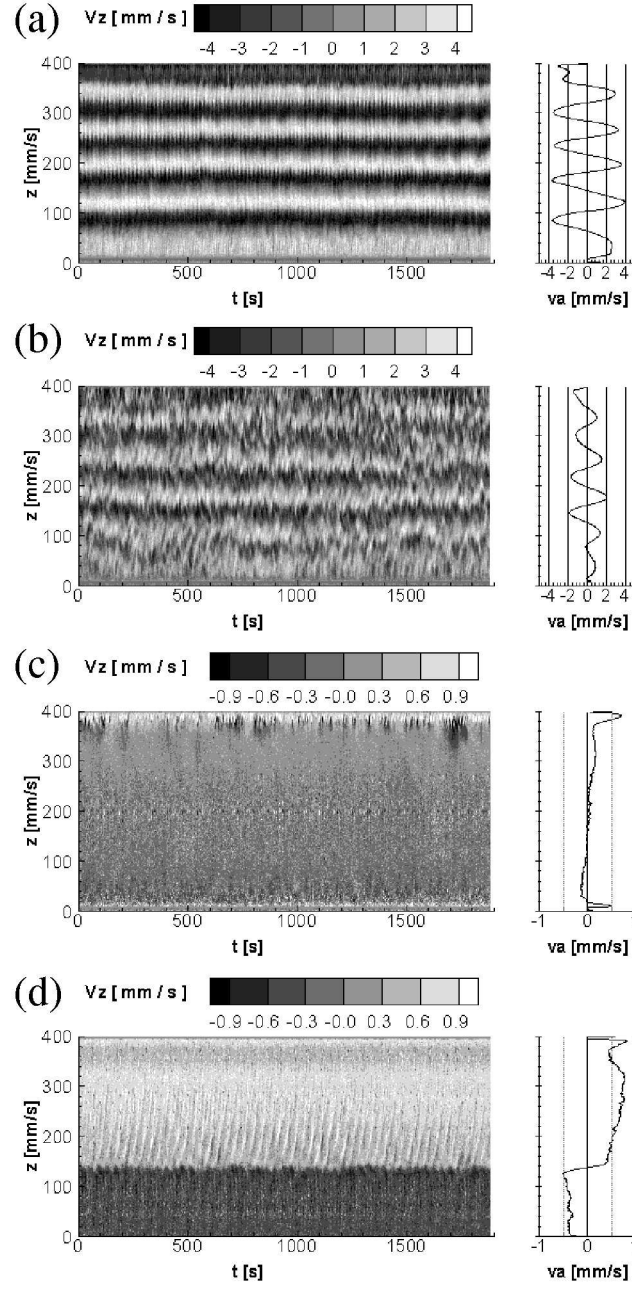


FIG. 3: Measured axial velocity  $V_z(z, t)$  (l.h.s.), and time averaged  $va_z(z)$  (r.h.s.), in the field-free case for PROMISE 2, at  $f_{in} = 0.1$  Hz: (a)  $\mu = 0$ , (b)  $\mu = 0.1$ , (c)  $\mu = 0.27$ . (d) The same for PROMISE 1 at  $f_{in} = 0.06$  Hz and  $\mu = 0.27$ .

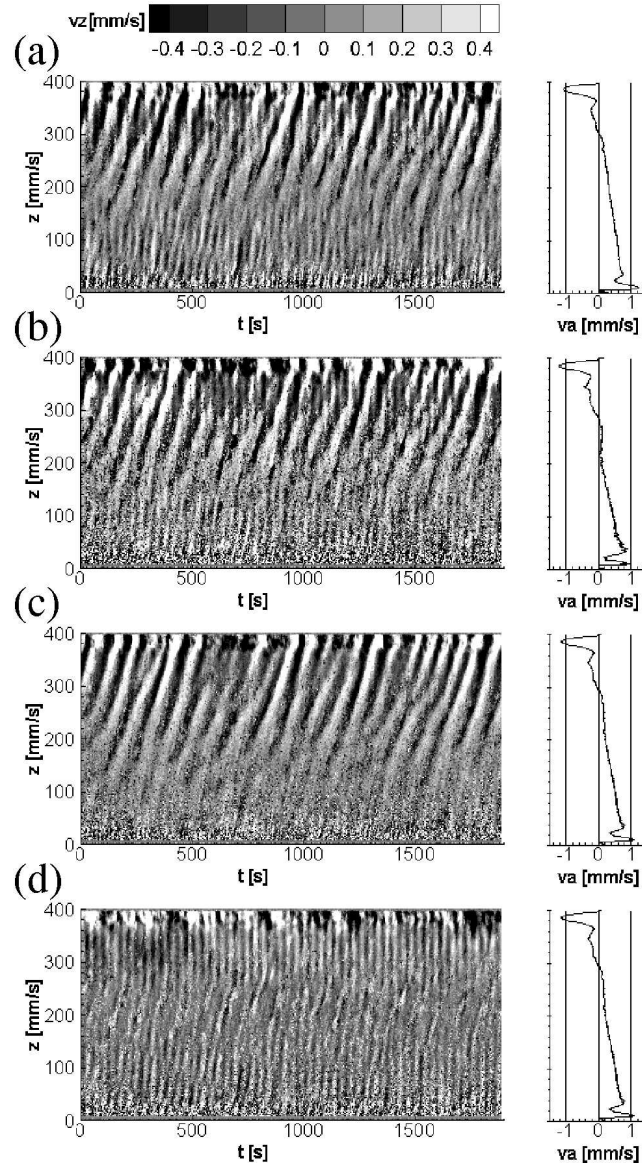


FIG. 4: Measured axial velocity for  $f_{\text{in}} = 0.1$  Hz,  $f_{\text{out}} = 0.027$  Hz,  $I_{\text{rod}} = 7000$  A, and  $I_{\text{coil}} = 76$  A. (a) at UDV sensor 1, (b) at UDV sensor 2, (c) average of sensor 1 and sensor 2, (d) difference of sensor 1 and sensor 2. The frequency seen in (d) is just the rotation rate of the outer cylinder.

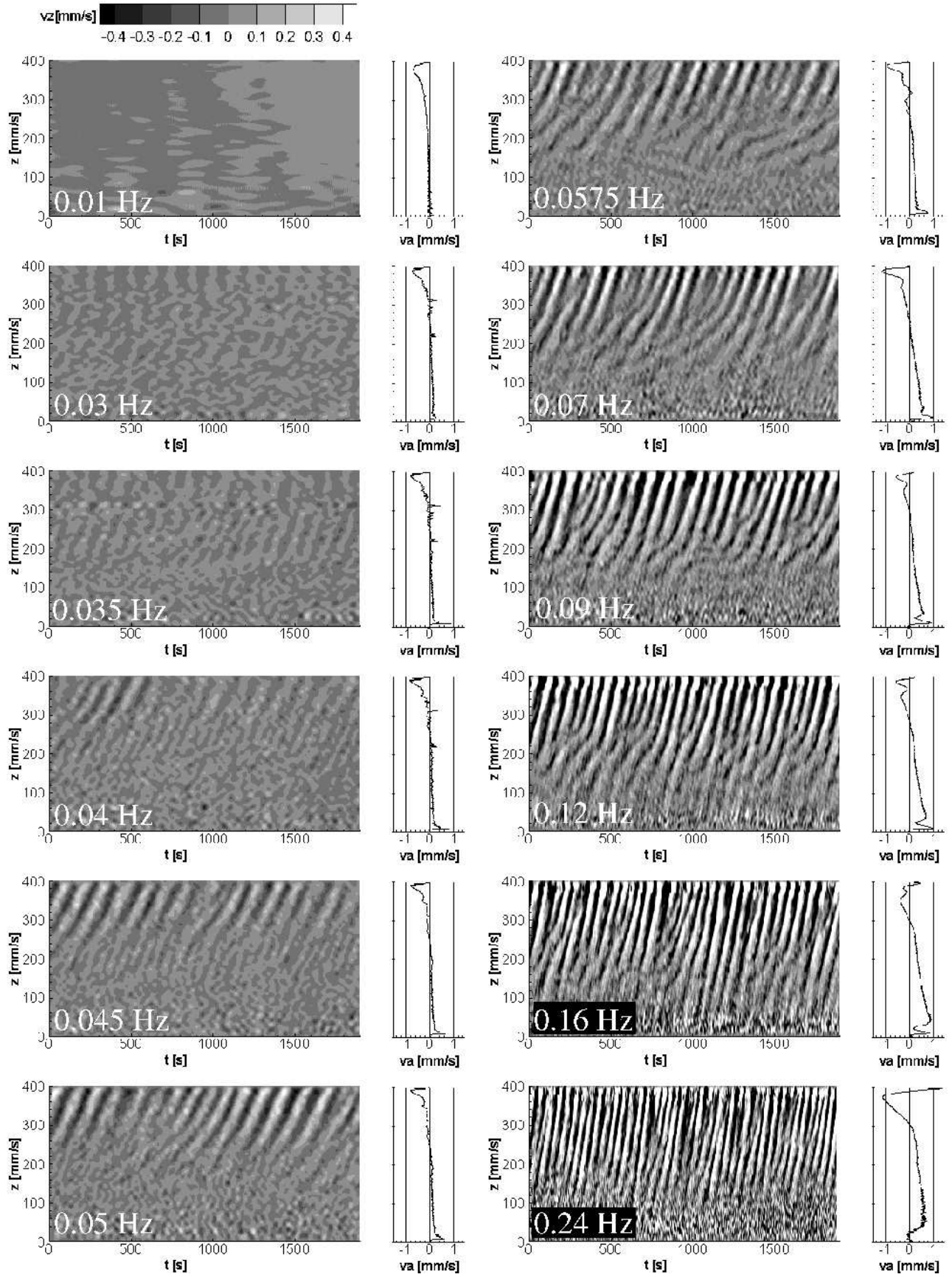


FIG. 5:  $v_z(z,t)$  and  $v_a(z,t)$ , both averaged over the two UDV sensors, in dependence on  $f_{in}$  (i.e.  $Re$ ) for  $\mu = 0.27$ ,  $I_{rod} = 7000$  A, and  $I_{coil} = 76$  A.

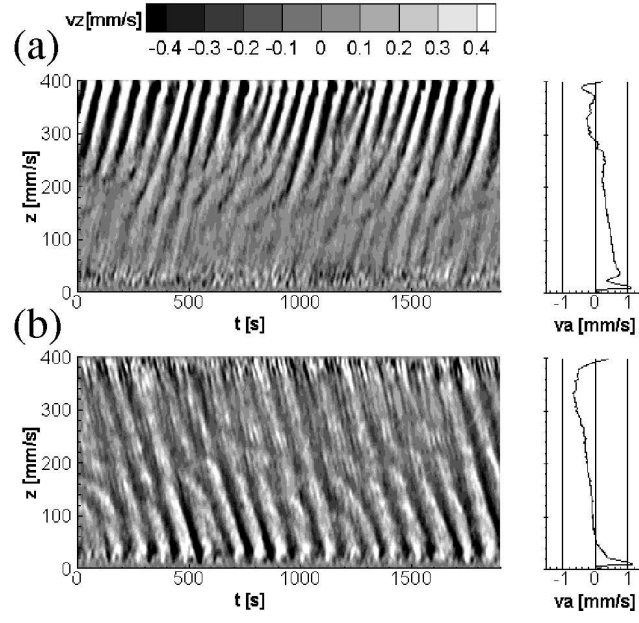


FIG. 6:  $v_z(z, t)$  and  $v_{a_z}(z)$ , both averaged over the two UDV sensors, for  $f_{\text{in}} = 0.1$  Hz,  $\mu = 0.27$ ,  $I_{\text{rod}} = 7000$  A: (a)  $I_{\text{coil}} = 76$  A, (b)  $I_{\text{coil}} = -76$  A. The change of the current direction in the coil makes the MRI wave change its direction from (a) upward to (b) downward.

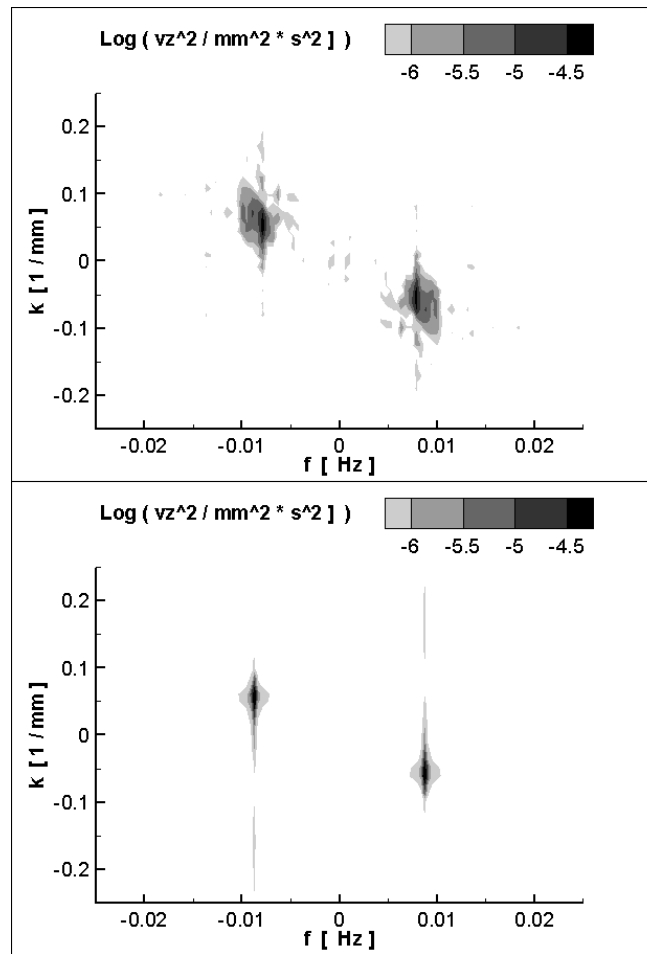


FIG. 7: Power spectral density of the 2D FFT of  $v_z(z, t)$  for  $f_{\text{in}} = 0.05$  Hz,  $\mu = 0.27$ ,  $I_{\text{rod}} = 7000$  A, and  $I_{\text{coil}} = 76$  A. Upper panel: experimental results, Lower panel: results of the simulation with a 2D solver.

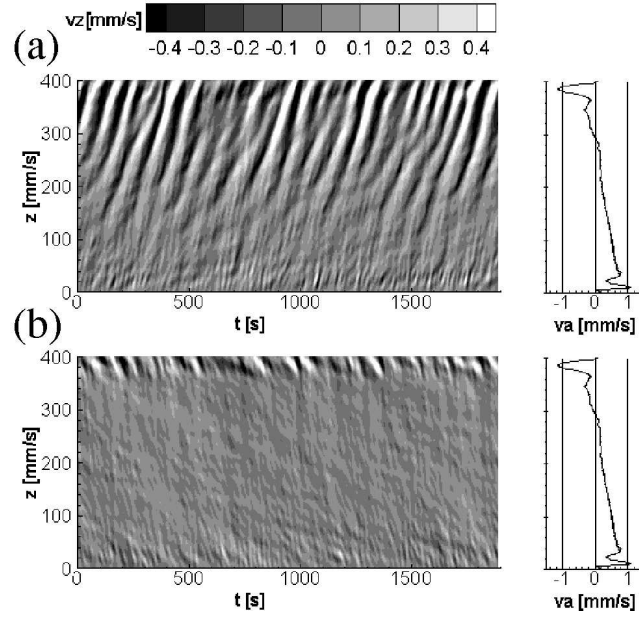


FIG. 8:  $va_z(z)$  and Hilbert transforms of  $v_z(z, t)$  for  $f_{in} = 0.1$  Hz,  $\mu = 0.27$ ,  $I_{rod} = 7000$  A,  $I_{coil} = 76$  A. (a) Dominant upward travelling component, (b) minor downward travelling component which results from a reflection of the upward travelling component at the upper end-cap.

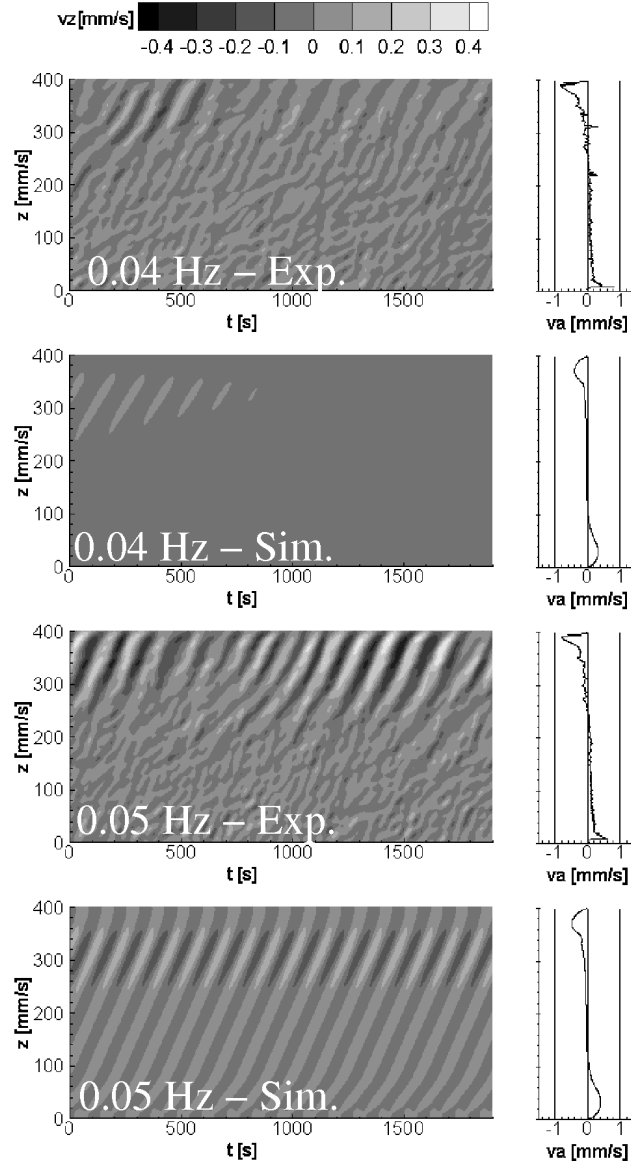


FIG. 9: Comparison of experimental and simulated results for the upward travelling wave component for  $\mu = 0.27$ ,  $I_{rod} = 7000$  A,  $I_{coil} = 76$  A,  $f_{in} = 0.04$  Hz (upper two panels) and  $f_{in} = 0.05$  Hz (lower two panels).

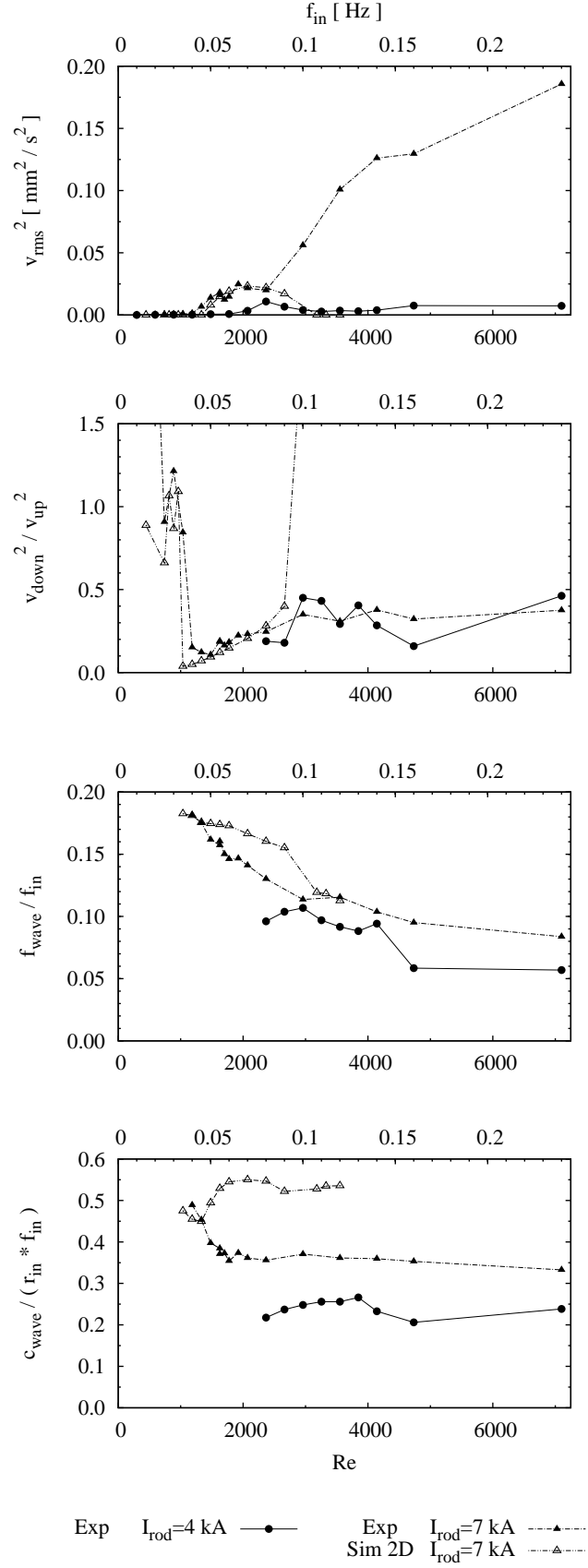


FIG. 10: Squared rms of  $v_z(z, t)$ , squared ratio of maximum amplitude of downward to upward travelling waves, normalized frequency and normalized wave speed for  $\mu = 0.27$ ,  $I_{rod} = 4000$  A and 7000 A,  $I_{coil} = 76$  A, in dependence on  $f_{in}$  (i.e.  $Re$ ).

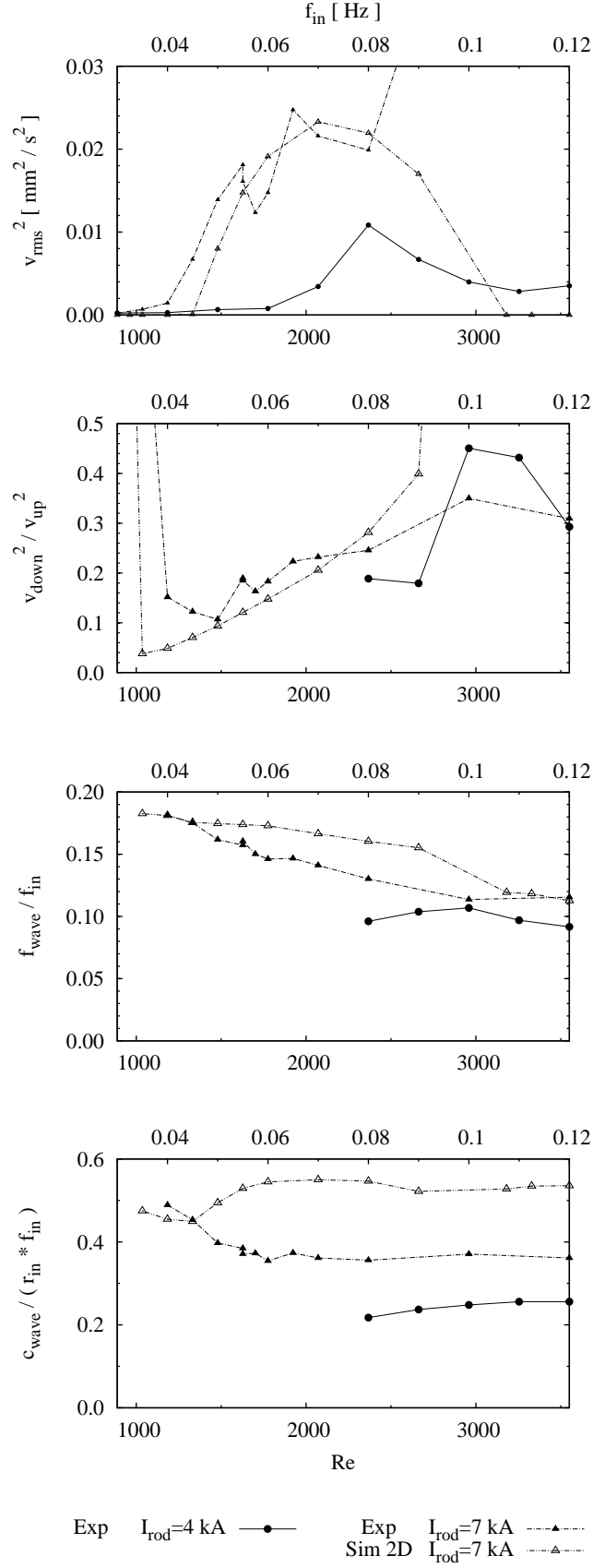


FIG. 11: Same as Fig. 10, but zoomed to medium values of  $f_{in}$ .

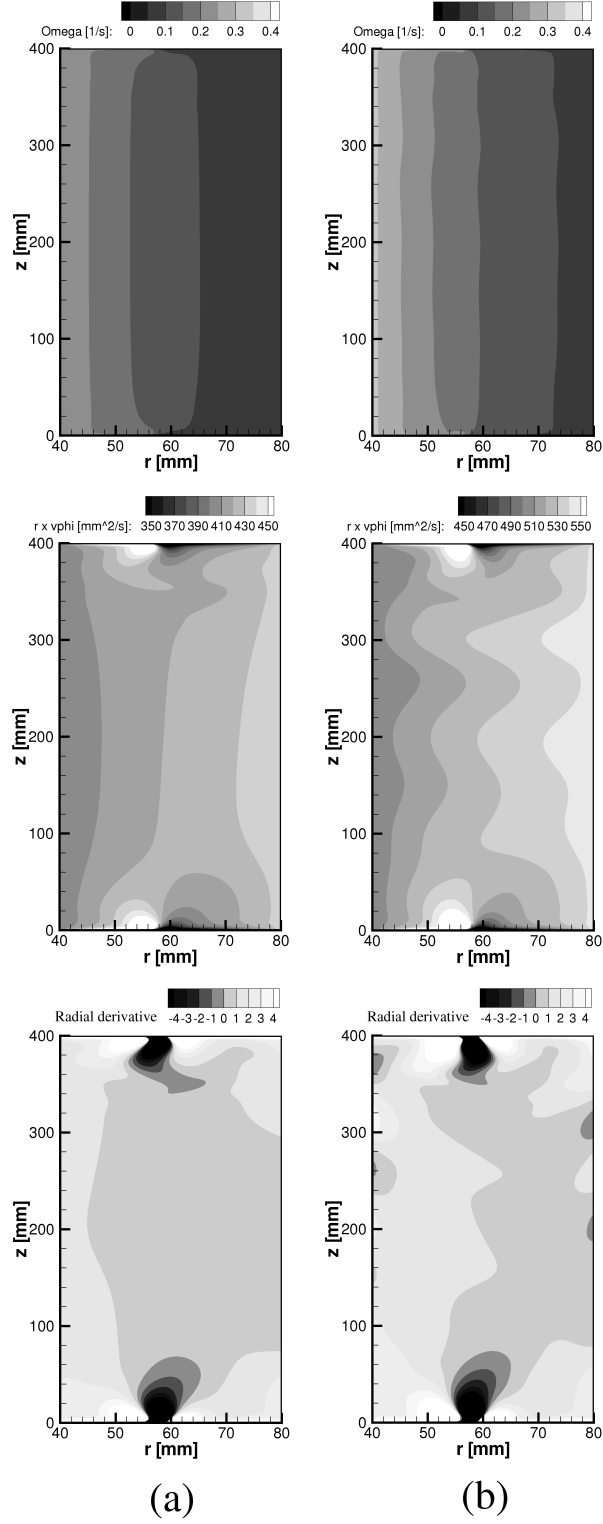


FIG. 12: From top to bottom: Simulated angular velocity  $\Omega(r, z)$ , specific angular momentum  $r^2 \Omega(r, z)$ , and radial derivative of  $r^2 \Omega(r, z)$  for  $\mu = 0.27$ ,  $I_{\text{rod}} = 7000$  A,  $I_{\text{coil}} = 76$  A. (a) Subcritical  $f_{\text{in}} = 0.04$  Hz. (b) Supercritical  $f_{\text{in}} = 0.05$  Hz.

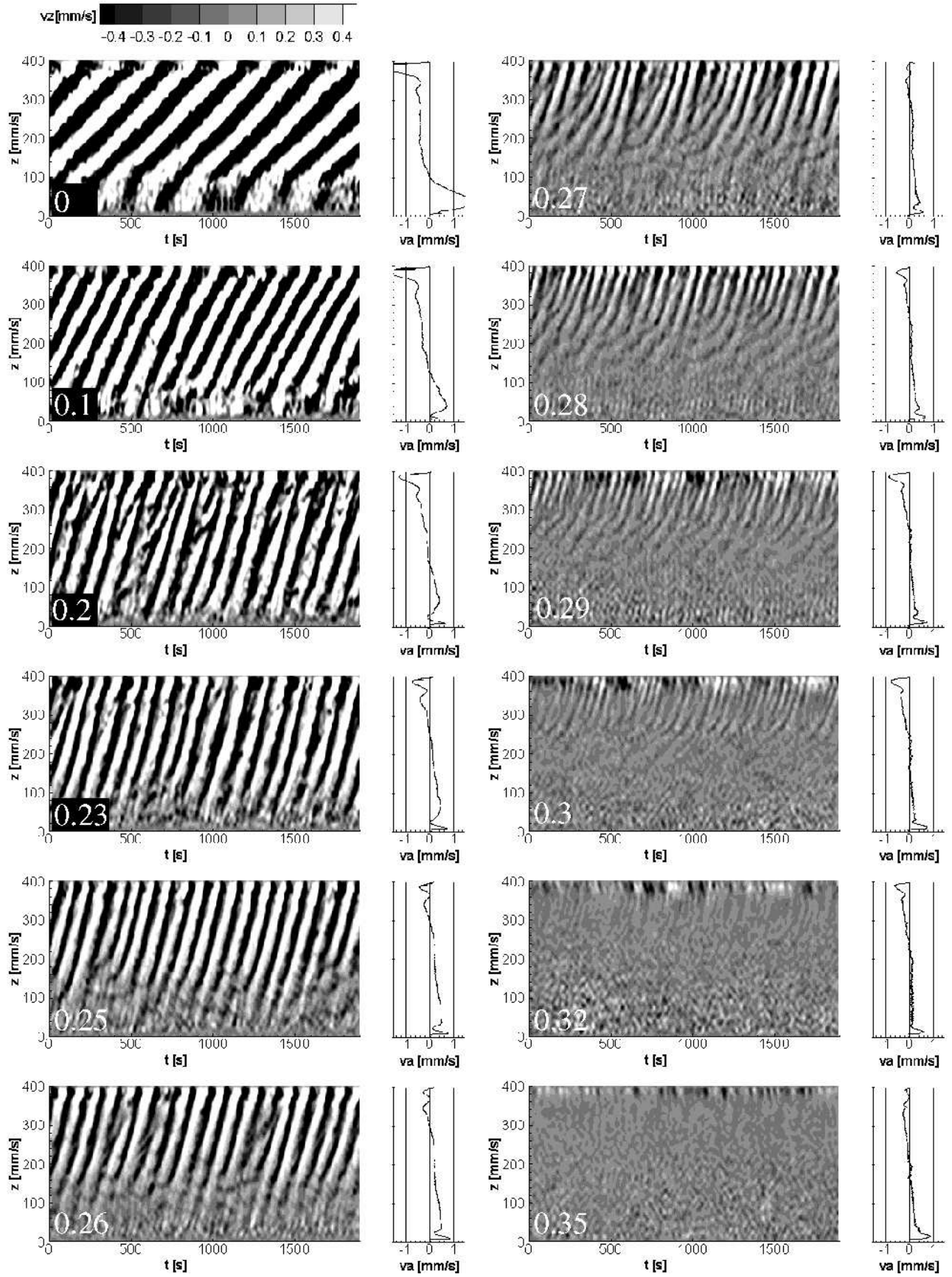


FIG. 13:  $v_z(z, t)$  and  $v_a(z)$ , both averaged over the two UDV sensors, in dependence on  $\mu$  for  $f_{in} = 0.1$  Hz,  $I_{rod} = 7000$  A, and  $I_{coil} = 76$  A.

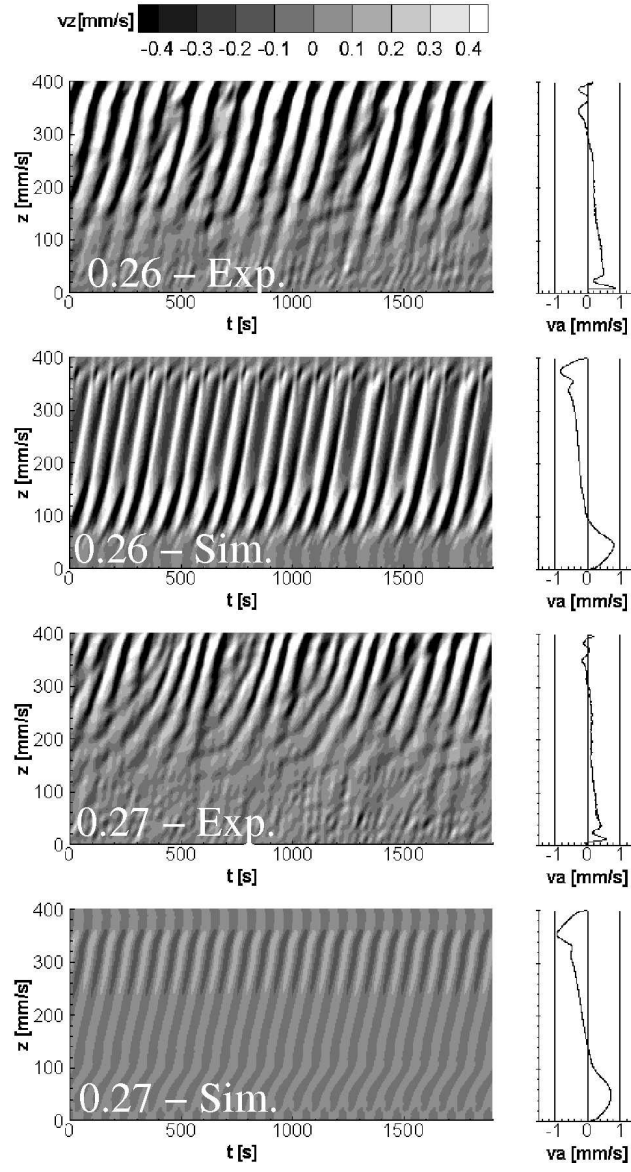


FIG. 14: Comparison of experimental and simulated results for the upward travelling wave component for  $f_{in} = 0.1$  Hz,  $I_{rod} = 7000$  A,  $I_{coil} = 76$  A,  $\mu = 0.26$  (upper two panels) and  $\mu = 0.27$  (lower two panels).

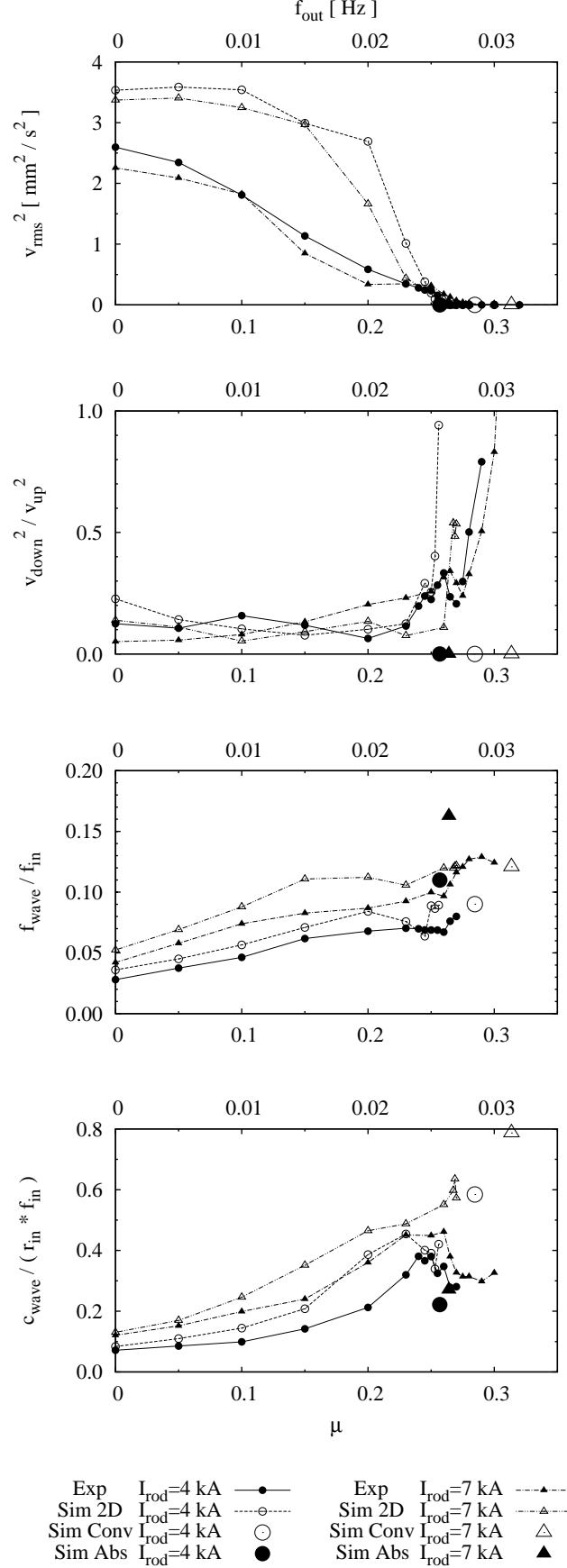


FIG. 15: Squared rms of  $v_z(z, t)$ , squared ratio of maximum amplitude of downward to upward travelling waves, normalized frequency and normalized wave speed for  $f_{in} = 0.1$  Hz,  $I_{rod} = 4000$  A and  $7000$  A,  $I_{coil} = 76$  A, in dependence in  $\mu$ .

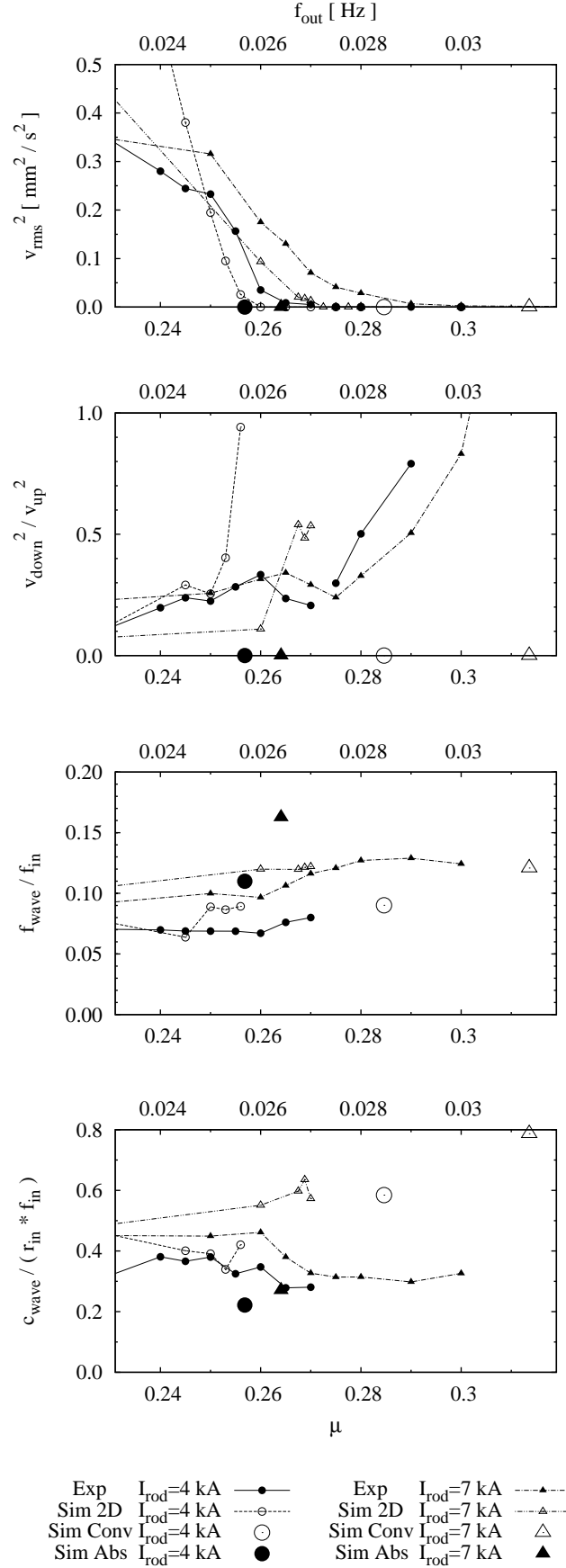


FIG. 16: Same as Fig. 15, but zoomed to  $\mu$  values close to the Rayleigh point  $\mu_{Ray1} = 0.25$ .

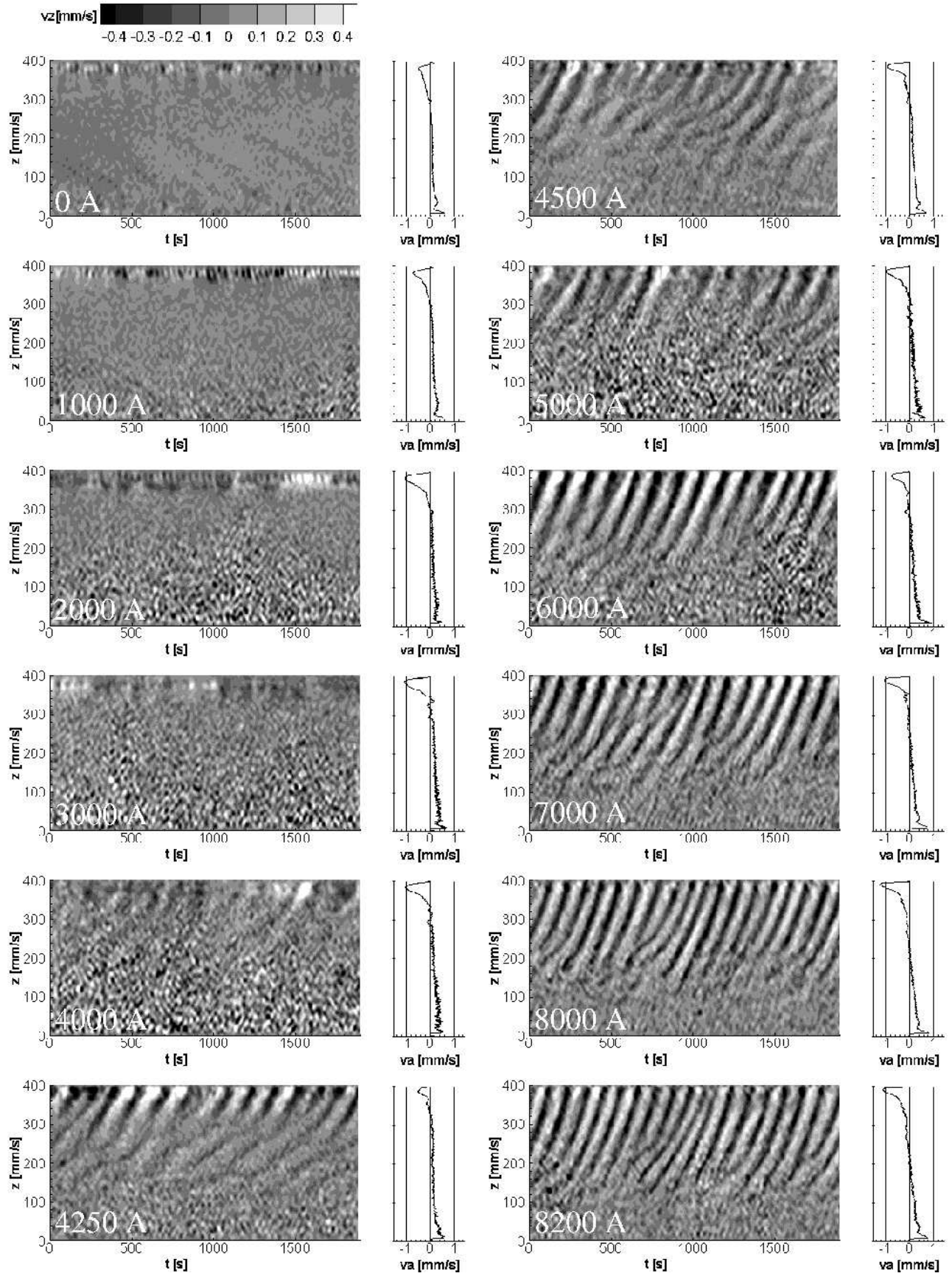


FIG. 17:  $v_z(z,t)$  and  $v_{a_z}(z)$ , both averaged over the two UDV sensors, in dependence on  $\beta$  for  $f_{in} = 0.06$  Hz,  $\mu = 0.26$ , and  $I_{coil} = 76$  A.

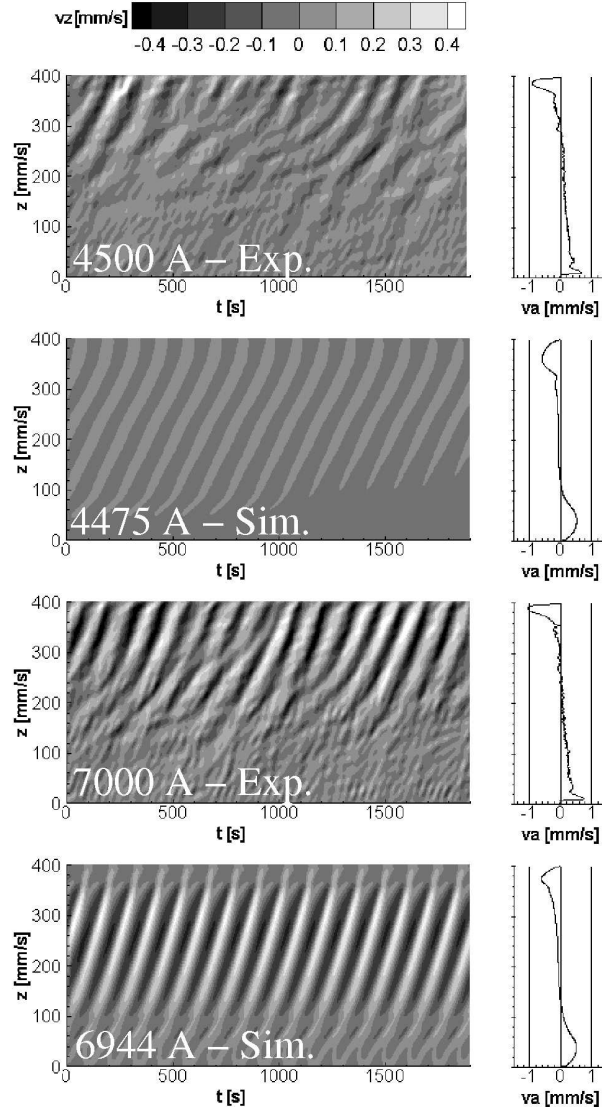


FIG. 18: Comparison of experimental and simulated results for the upward travelling wave components for  $f_{\text{in}} = 0.06$  Hz,  $\mu = 0.26$ , and  $I_{\text{coil}} = 76$  A,  $I_{\text{rod}} \sim 4500$  A (upper two panels) and  $I_{\text{rod}} \sim 7000$  A (lower two panels).

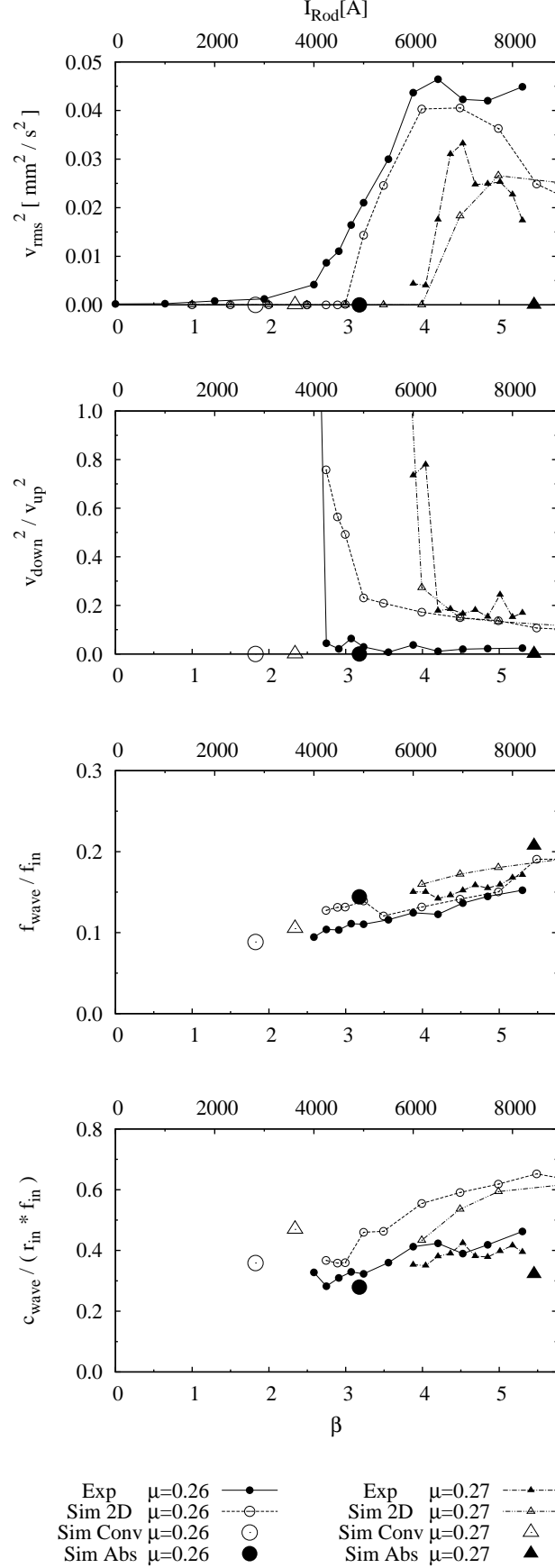


FIG. 19: Squared rms of  $v_z(z, t)$ , squared ratio of maximum amplitude of downward to upward travelling waves, normalized frequency and normalized wave speed for  $f_{\text{in}} = 0.06$  Hz,  $\mu = 0.26$  and  $0.27$ ,  $I_{\text{coil}} = 76$  A, in dependence on  $I_{\text{rod}}$  (i.e.  $\beta$ ).

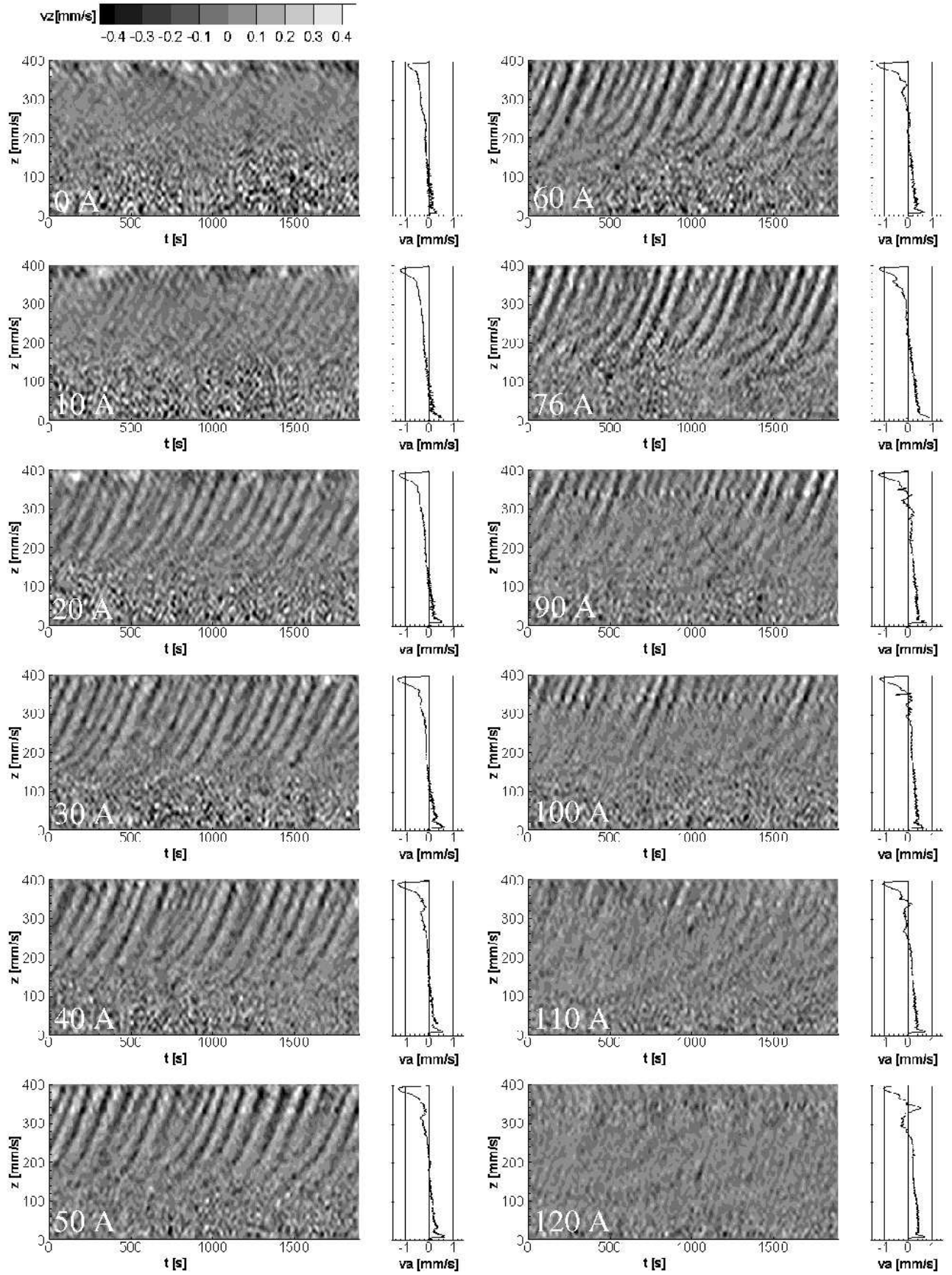


FIG. 20:  $v_z(z, t)$  in dependence on  $I_{\text{coil}}$  (i.e.  $Ha$ ) for  $f_{\text{in}} = 0.06$  Hz,  $\mu = 0.27$ , and  $I_{\text{rod}} = 8000$  A.

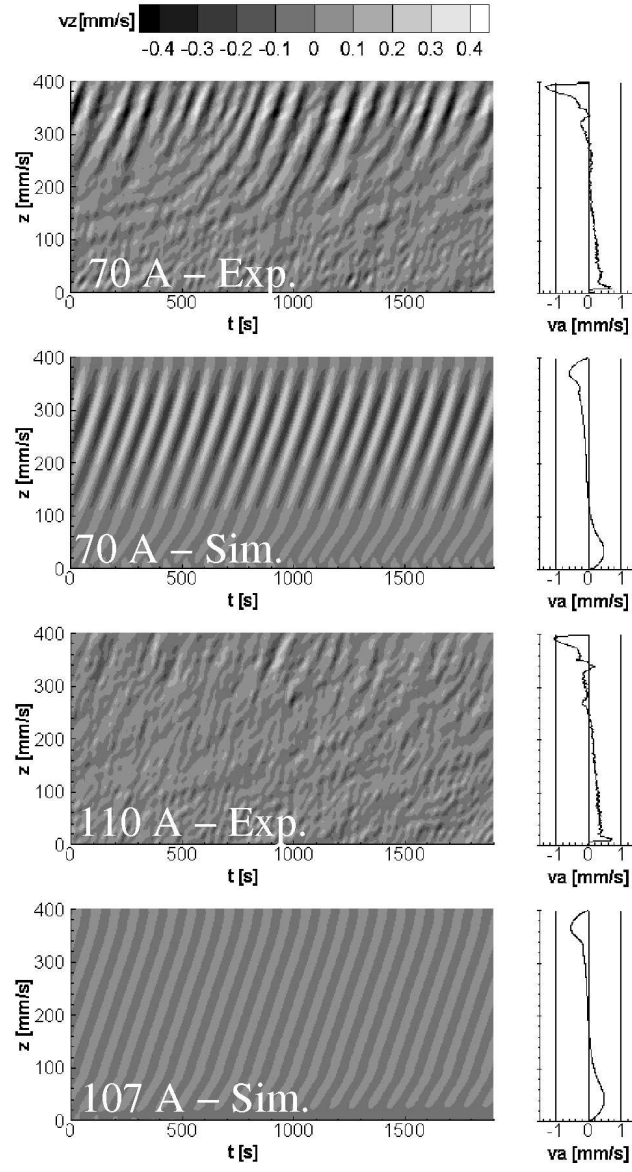


FIG. 21: Comparison of experimental and simulated results for the upward travelling wave components for  $f_{in} = 0.06$  Hz,  $\mu = 0.27$ , and  $I_{rod} = 8000$  A,  $I_{coil} = 70$  A and  $I_{coil} \sim 110$  A.

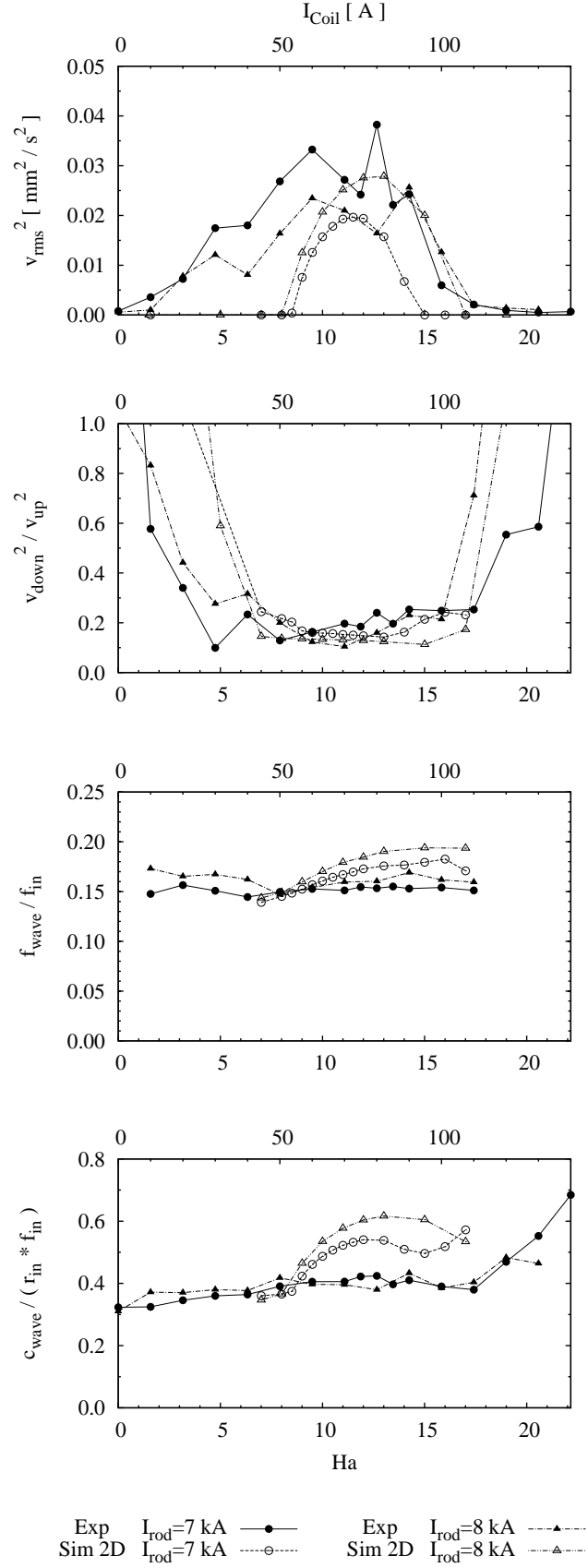


FIG. 22: Squared rms of  $v_z(z, t)$ , squared ratio of maximum amplitude of downward to upward travelling waves, normalized frequency and normalized wave speed for  $f_{\text{in}} = 0.06 \text{ Hz}$ ,  $\mu = 0.27$ ,  $I_{\text{rod}} = 7000 \text{ A}$  and  $8000 \text{ A}$ , in dependence on  $I_{\text{coil}}$  (i.e.  $Ha$ ).